scientific reports

Check for updates

OPEN

Regional quantification of metabolic liver function using hyperpolarized [1-^{13}C] pyruvate MRI

Uffe Kjaergaard[1,2,3]✉, Andrea Lund[2], Mohsen Redda[1], Mattias Hedegaard Kristensen[1], Malene Aastrup[1], Nikolaj Bøgh[1], Kim Sivesgaard[4], Michael A. Ohliger[5], Daniel B. Vigneron[5], Lotte Bonde Bertelsen[1], Aage Kristian Olsen Alstrup[6,7], Esben Søvsø Szocska Hansen[1], Frank Viborg Mortensen[2] & Christoffer Laustsen[1]

Assessment of liver function is essential before partial hepatectomy to predict the risk of post hepatectomy liver failure, a severe and life-threatening complication. Traditional methods have focused on expected future liver remnant (FLR) volume estimation. However, liver volume does not always correlate with function. We suggest that metabolism might be a better surrogate for function than volume. Therefore, we aimed to investigate the metabolic changes in a porcine model of partial portal vein ligation (PVL) using hyperpolarized magnetic resonance imaging (HP-MRI). Specifically, we sought to quantify and compare the pyruvate metabolism in the FLR and the deportalized liver (DL).

Six pigs underwent PVL. HP-MRI with [1-^{13}C] pyruvate was performed at baseline, post-surgery, and 1 week after surgery. Metabolic conversion was quantified with kinetic modelling of the rate constants of pyruvate to lactate (k_{PL}) and pyruvate to alanine (k_{PA}). Mean k_{PL} was increased in FLR compared to DL at post-surgery and 1 week after surgery ($P = 0.002$), while k_{PA} was unaltered ($P = 0.761$). These findings indicate a metabolic shift towards glycolysis in the FLR. This non-invasive metabolic imaging technique could serve as a powerful tool for evaluation of regional liver function prior to partial hepatectomy and consequently improve patient outcomes.

Keywords Magnetic resonance imaging, Hyperpolarized, Lactate dehydrogenase (LDH), Alanine aminotransferase (ALT), Liver regeneration, Portal vein ligation, Post-hepatectomy liver failure (PHLF), Gadoxetate-enhanced imaging, Metabolic imaging, Hepatic function, Translational

Abbreviations

ADC	Apparent diffusion coefficient
A.U.	Arbitrary units
ALPPS	Associating liver partition and portal vein ligation for staged hepatectomy
ALT	Alanine aminotransferase
CL	Caudate lobe
DCE	Dynamic contrast enhancement
DL	Deportalized liver
DWI	Diffusion-weighted imaging
FLR	Future liver remnant
FOV	Field of view
HA	Hepatic artery
HP-MRI	Hyperpolarized magnetic resonance imaging

[1]MR Research Centre, Department of Clinical Medicine, Aarhus University, Aarhus, Denmark. [2]Department of Surgery, Section for HPB Surgery, Aarhus University Hospital, Palle Juul-Jensens Boulevard 99, Aarhus N 8200, Denmark. [3]Department of Surgery, Horsens Regional Hospital, Horsens, Denmark. [4]Department of Radiology, Department of Clinical Medicine, Aarhus University Hospital, Aarhus, Denmark. [5]Department of Radiology and Biomedical Imaging, University of California, San Francisco, CA, USA. [6]Department of Nuclear Medicine and PET, Aarhus University Hospital, Aarhus, Denmark. [7]Department of Clinical Medicine, Aarhus University, Aarhus, Denmark. ✉email: uffe@clin.au.dk

k_{PA}	Pyruvate-to-alanine conversion rate constant
k_{PL}	Pyruvate-to-lactate conversion rate constant
LDH	Lactate dehydrogenase
LM	Left medial
LL	Left lateral
MCT1	Monocarboxylate transporter 1
MCT4	Monocarboxylate transporter 4
MTT	Mean transit time
OATP	Organic anion transporting polypeptide
PDH	Pyruvate dehydrogenase
PHLF	Post-hepatectomy liver failure
PVE	Portal vein embolization
PV	Portal vein
PVL	Partial portal vein ligation
RLE	Relative liver enhancement
RL	Right lateral
RM	Right medial
ROI	Region of interest
TE	Echo time
TR	Repetition time
TTP	Time to peak

Partial hepatectomy remains a cornerstone in the curative treatment of liver malignancies, offering the potential for long-term survival[1,2]. However, one of the major concerns associated with this procedure is post-hepatectomy liver failure (PHLF), a life-threatening complication that can significantly impact patient outcomes. Therefore, preoperative assessment of liver function is crucial before major partial hepatectomy to avoid PHLF[3,4].

The liver's unique regenerative ability is a prerequisite for all major liver resections. Liver regeneration is predominantly driven by the proliferation and hypertrophy of hepatocytes[5,6]. This regenerative activity is highly energy-intensive and necessitates a metabolic shift towards glycolysis, similar to the Warburg effect observed in cancer cells[7]. Techniques such as portal vein embolization (PVE), partial portal vein ligation (PVL), or two-stage partial hepatectomy and associating liver partition with PVL for staged hepatectomy (ALPPS) significantly reduce the risk of PHLF by allowing the future liver remnant (FLR) to regenerate between stages and thereby increasing volume before the final resection[8,9].

Traditionally, FLR volume estimation, using CT or MRI, has been the primary method for assessing PHLF risk. Higher FLR volumes correlate strongly with reduced PHLF risk[10]. However, liver volume does not always accurately reflect liver function. Therefore, PHLF remains a significant challenge, especially in patients with compromised liver parenchyma[11]. Current preoperative assessment of liver function primarily relies on clinical scoring systems, such as the Child-Pugh and MELD scores, which are not quantitative[12,13]. Dynamic tests, including the indocyanine green clearance and LiMAx ^{13}C-methionine breath tests, provide valuable insights but do not offer regional specificity[14–16]. Recent advancements in imaging techniques, such as MRI with gadoxetate disodium and ^{99m}Tc-mebrofenin SPECT, have demonstrated potential for evaluating regional liver function and providing a more localized assessment of hepatic capacity[17–20]. However, these imaging modalities do not capture dynamic functional changes, and ^{99m}Tc-mebrofenin SPECT involves exposure to ionizing radiation.

Hyperpolarized [1-^{13}C] pyruvate MRI offers a novel and powerful tool to non-invasively study metabolic processes, including glycolysis, in vivo, providing real-time insights into pyruvate uptake and conversion into its metabolic products lactate, alanine and bicarbonate[21]. Thus, it enables quantification of the enzymatic activity responsible for these conversions (Lactate dehydrogenase (LDH), alanine aminotransferase (ALT), pyruvate dehydrogenase (PDH), respectively). Furthermore, the regional distribution of these processes can be displayed to selectively study the FLR vs. DL. Previously the method has been used to assess liver metabolism in preclinical studies[22–25] and in humans[26,27]. A single study assessed metabolism in liver regeneration in a mouse model after 70% hepatectomy[32].

This study aims to utilize hyperpolarized [1-^{13}C] pyruvate MRI to investigate the metabolic alterations in a porcine model of PVL, with the goal of better replicating human physiology. By quantifying the pyruvate to lactate conversion, we seek to elucidate the metabolic shifts that underpin liver regeneration. With this advanced imaging technique, we aim to provide a more detailed understanding of the metabolic changes occurring in the FLR post-PVL, potentially leading to improved strategies for predicting and evaluating liver regeneration, thereby reducing the risk of PHLF.

Results

Hyperpolarized [1-^{13}C] metabolism following PVL

Representative MRI and HP-MRI are presented in Fig. 1. At baseline, mean k_{PL} values were not different between DL and FLR, as expected (0.092 s^{-1} (95% CI: [0.059, 0.125]) versus 0.096 s^{-1} (95% CI: [0.065, 0.126]). Post-surgery, mean k_{PL} values decreased in DL while increasing in FLR (0.070 s^{-1} for DL (95% CI: [0.060, 0.080]) versus 0.112 s^{-1} (95% CI: [0.090, 0.133])). These changes persisted after 1 week, with mean k_{PL} values remaining lower in DL (0.081 s^{-1}, 95% CI: [0.053, 0.109]) and elevated in FLR (0.110 s^{-1}, 95% CI: [0.080, 0.141], Fig. 2A). Mixed effect analysis of k_{PL}, showed a significant interaction between liver regions and time ($F(2, 10) = 12.3$, $P = 0.002$). However, there was no significant effect of liver regions ($P = 0.908$), while there was a significant effect of time ($P = 0.004$). In contrast, for k_{PA}, there was no significant interaction between liver regions and time ($F(2, 6) = 0.286$, $P = 0.761$; Fig. 2B).

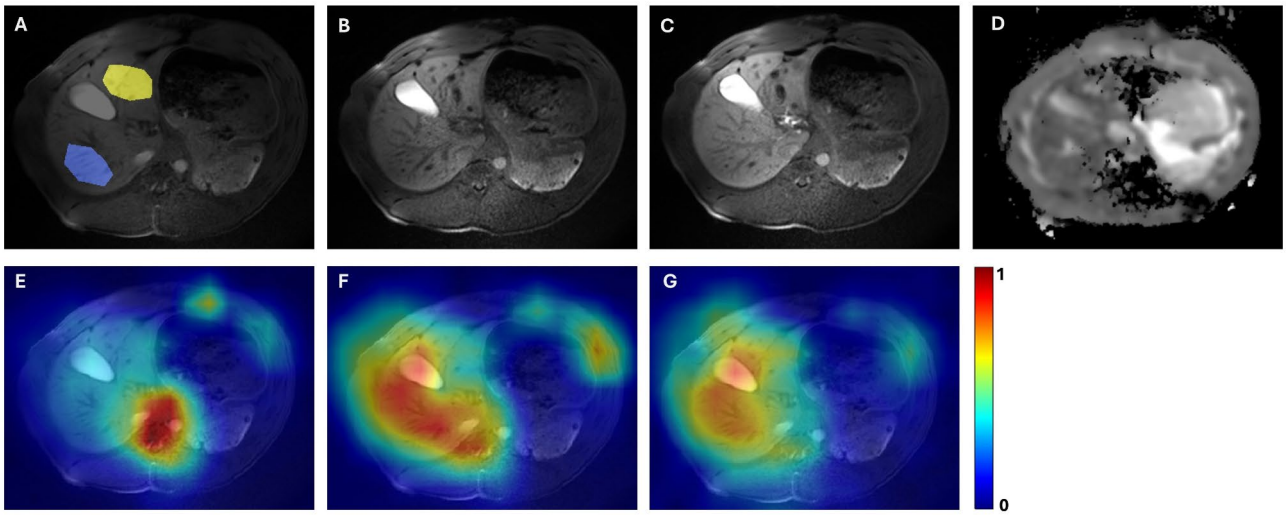

Fig. 1. MR images from one pig post-surgery. (**A**) T1-weighted dual-echo spoiled gradient echo imaging with ROIs placements (yellow is DL, blue is FLR), (**B**) T1-weighted dual-echo spoiled gradient echo before gadoxetate disodium injection, (**C**) T1-weighted 20 min after gadoxetate disodium injection, (**D**) ADC map, (**E**–**G**) Raw intensity maps summed over the whole acquisition time (112 s), for pyruvate (**E**), lactate (**F**) and alanine (**G**); overlayed on T1-weighted proton images. For visualization ^{13}C maps are linearly interpolated to in-plane resolution of 1H images before overlay. Pyruvate is downscaled by a factor 2 and alanine upscaled by a factor 2.

ADC and RLE

At baseline, mean ADC for DL and FLR was similar (1514.82×10^{-6} mm^2/s (95% CI: [1405.13, 1624.50] versus 1436.36×10^{-6} mm^2/s (95% CI: [1323.16, 1549.56]). Post-surgery, mean ADCs were 1549.76×10^{-6} mm^2/s for DL (95% CI: [1469.09, 1630.43]) and 1429.92×10^{-6} mm^2/s for FLR (95% CI: [1284.12, 1575.73]). After 1 week, mean ADCs were 1707.91×10^{-6} mm^2/s for DL (95% CI: [1531.44, 1884.38]) and 1379.99×10^{-6} mm^2/s for FLR (95% CI: [1189.43, 1570.56]) (Fig. 2C). There was a significant interaction between liver regions and time on mean ADC ($F(2, 9) = 5.96$, $P = 0.023$; Fig. 2C). The main effect of time was significant ($P = 0.004$), but the main effect of liver regions was not ($P = 0.556$). Mean RLE for DL was 50.70% at baseline (95% CI: [42.04%, 59.37%]), while for FLR it was 65.43% (95% CI: [46.80%, 84.07%]). Post-surgery, mean RLEs were 48.54% for DL (95% CI: [27.69%, 69.38%]) and 60.66% for FLR (95% CI: [41.32%, 80.00%]). After 1 week, mean RLEs were 43.96% for DL (95% CI: [24.06%, 63.86%]) and 63.29% for FLR (95% CI: [55.87%, 70.70%]) (Fig. 2D). The mixed-effects analysis revealed no significant interaction between time and liver regions on RLE ($P = 0.686$, $F(2, 8) = 0.396$). Additionally, there was no significant effect of time on RLE ($P = 0.881$). However, a significant effect of liver regions was observed ($P = 0.007$).

Hemodynamic analysis

Gadoxetate hemodynamic analysis showed no significant interaction between liver regions and time in TTP ($P = 0.744$), MTT ($P = 0.951$), skewness ($P = 0.770$) or kurtosis ($P = 0.561$) (Figs. 3 and 4, and Supplementary Materials and methods; Table S2). In the DL following PVL, there was a decrease in TTP for lactate ($P = 0.027$), while no significant changes were observed for TTP pyruvate ($P = 0.309$) and TTP alanine ($P = 0.359$). MTT pyruvate and lactate was lower in DL compared to FLR ($P = 0.031$ and $P = 0.013$, respectively), with a similar tendency for alanine ($P = 0.053$). Skewness was higher for all three metabolites in DL following PVL (pyruvate; $P = 0.017$, lactate; $P = 0.034$, alanine $P = 0.041$). For kurtosis, significant differences were noted for pyruvate ($P = 0.013$) and lactate ($P = 0.016$), but not for alanine ($P = 0.103$). The full statistical analysis, including P values and F-statistics for gadoxetate, pyruvate, alanine, and lactate, is available in Supplementary Materials and methods; Table S2.

Proliferation rate, hepatocyte volume, and mRNA expression

1 week after PVL, there were no changes in the relative mRNA expression levels of LDH, PDH, ALT, MCT1, and MCT4 (Fig. 5). Additionally, no changes in proliferation rate or mean hepatocyte volume were observed (Fig. 5).

Discussion

This study investigated the metabolic changes in a porcine model of PVL using HP-MRI. Key findings revealed a significant increase in k_{PL} in the FLR compared to the DL both within few hours after surgery and after 1 week. In contrast, there was no change in k_{PA} between the FLR and DL.

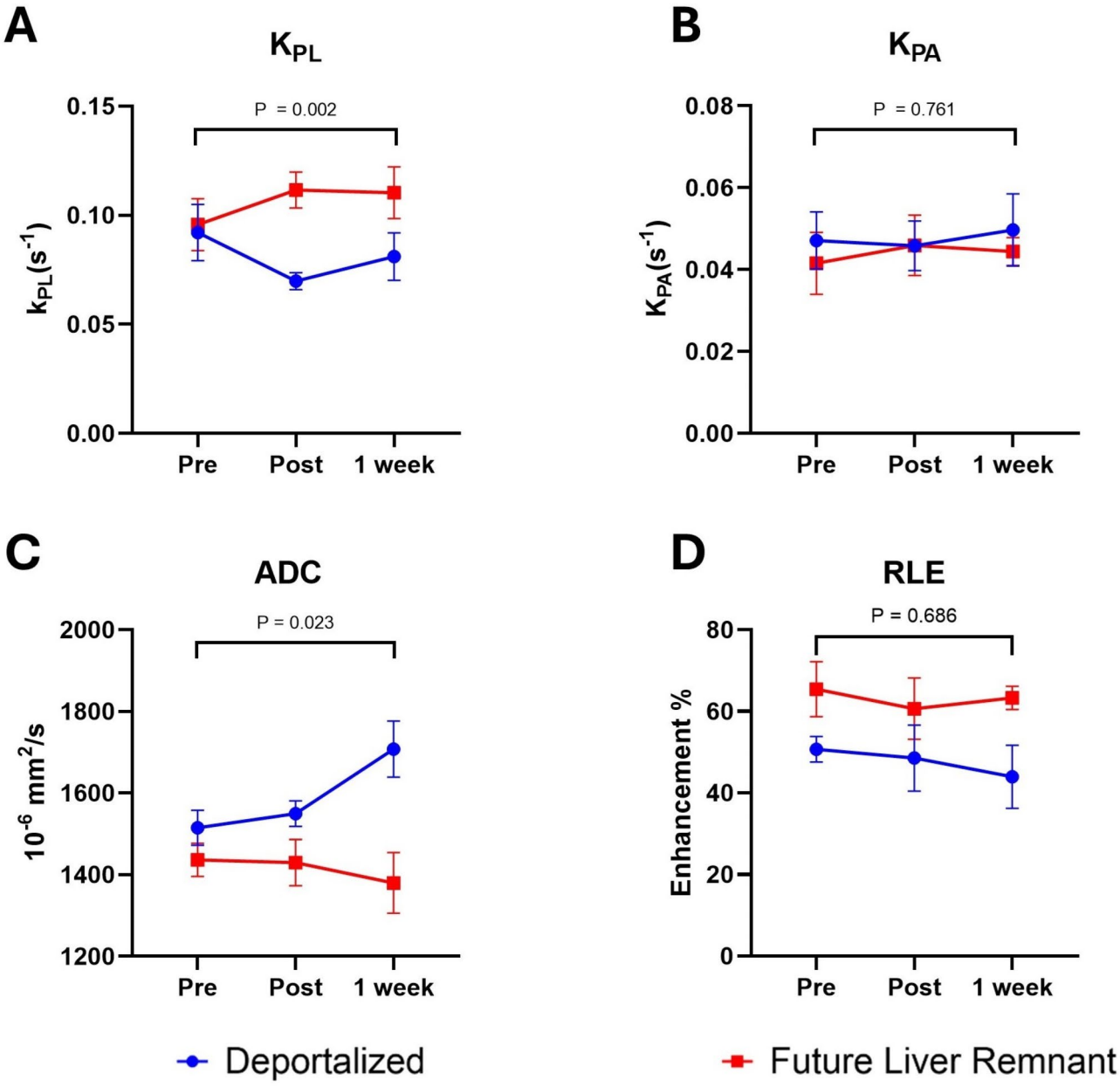

Fig. 2. Hyperpolarized and conventional MRI measurements in the liver. (**A**) Pyruvate to lactate conversion rate constant (k_{PL}) (P = 0.002), (**B**) Pyruvate to alanine conversion rate constant (k_{PA}) (P = 0.761). (**C**) Apparent diffusion coefficient (ADC) and (**D**) relative liver enhancement (RLE) 20 minutes after gadoxetic acid injection. An input less two site model was used for kinetic modeling of k_{PL} and k_{PA}. Effect over time and between deportalized and future liver remnant was analyzed with mixed-effects models. Sample size N = 6 (for k_{PA} pre and post sample size N=5).

Hyperpolarized pyruvate but not gadoxetate revealed altered hemodynamics after PVL

By ligating the portal vein branch the DL receives input only from the hepatic artery, while the FLR retains its dual input (Fig. 4A). For gadoxetate, no changes in perfusion parameters (TTP or MTT) or distribution parameters (skewness or kurtosis) could be demonstrated between FLR and DL (Figs. 3 and 4). For pyruvate, clear changes in MTT, skewness, and kurtosis were found between DL and FLR, while TTP remained unaltered, likely because of the biphasic curve in the FLR (Fig. 4A). Lactate was affected in all four parameters, while alanine was affected only in skewness. Similar tendencies were observed for kurtosis and MTT. However, it is important to address that gadoxetate is accumulating in the liver over time and therefore is likely to peak at the end of the DCE MRI scan, while the HP products rapidly decay (due to T1-relaxation, metabolic conversion and imaging). This might not be as apparent with extravascular contrast agents. We chose gadoxetate over extravascular agents because of its ability to assess liver function with RLE in the hepatobiliary phase[28]. However, in this study RLE was not different between FLR and DL following PVL, suggesting that the organic anion transporting polypeptides

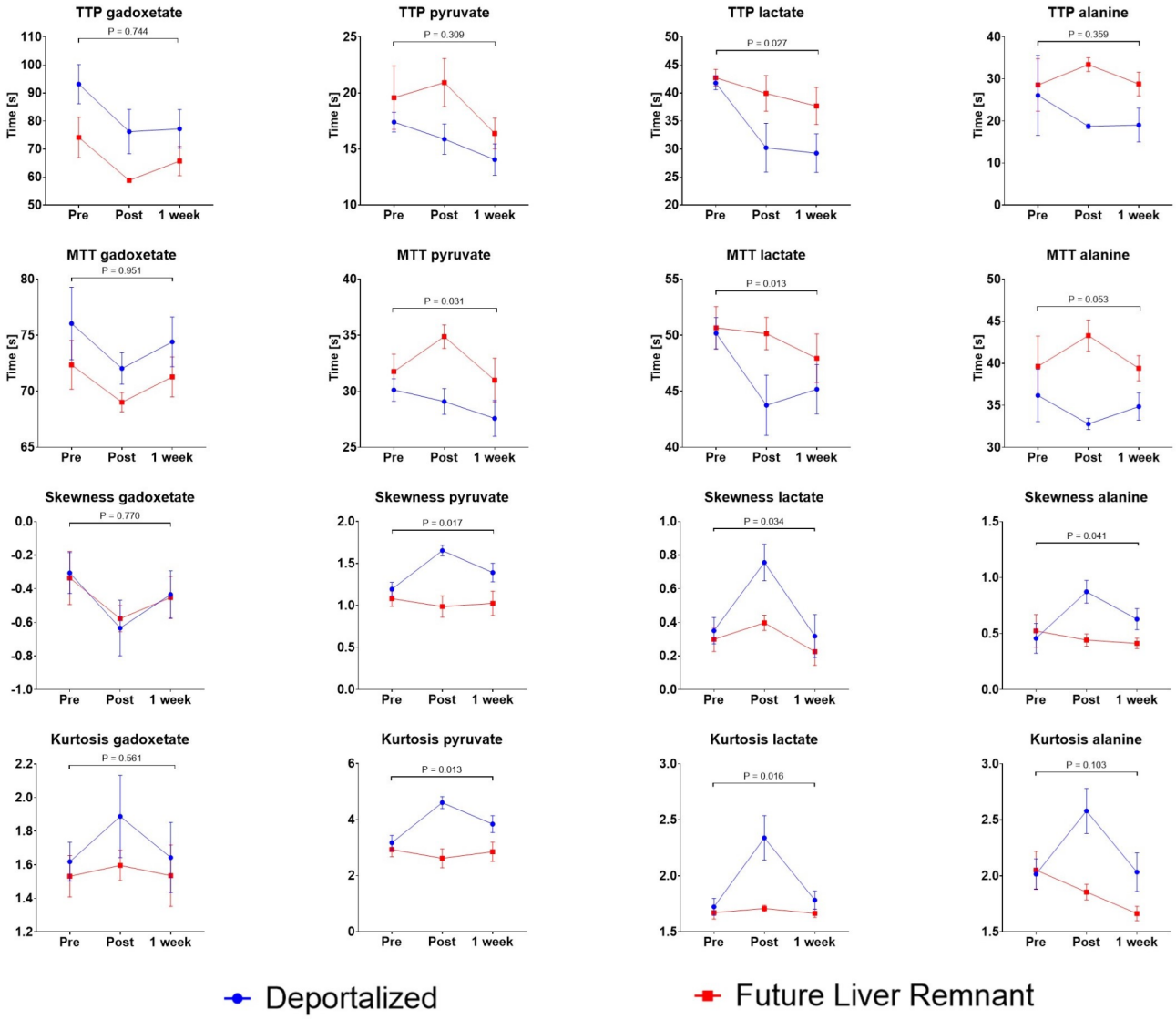

Fig. 3. Hemodynamic analysis of HP-MRI and DCE-MRI. MTT, TTP, skewness and kurtosis for gadoxetate, pyruvate, lactate and alanine pre-, post-surgery and 1 wk after surgery. P-values represent the interaction between liver regions and time. Tested using linear mixed-effects models. For full statistical analysis see Supplementary Materials & methods; Table S2. *MTT* mean transit time, *TTP* time to peak.

(OATP) responsible for uptake of gadoxetate into hepatocytes and/or release into bile by multidrug resistance-associated protein (MRP) were not affected and that the hepatocyte uptake of gadoxetate in practice displays zero-order kinetics i.e. is unaffected by perfusion changes. The significant effect of liver regions observed in RLE is likely associated with inhomogeneity of coil sensitivity, which is more pronounced in the posterior part where the FLR is anatomically placed. Since no significant interaction on RLE between liver regions and time was found, this systematic error did not directly influence our results. The discrepancy between gadoxetate and HP-MRI in assessing both hemodynamic changes and liver function highlights the added value of HP-MRI in a clinical setting. Our results suggest that HP-MRI is more sensitive to changes in liver function and alterations in arterial/portal blood supply than gadoxetate-enhanced MRI, which is particularly relevant for hepatocellular carcinoma, where relative arterial supply is increased due to angiogenesis[29].

ADC following PVL

ADC increased in DL compared to FLR following PVL, with the greatest difference observed after 1 week (Fig. 2C). The higher mean ADC value in DL could be due to cardiac motion or insufficient respiration gating[30], however it is unlikely to explain the large difference observed after 1 week. The anatomy did not allow alternating ligation of liver lobes to avoid this issue. An increase in the cell density, due to increase in hepatocytes in the FLR with subsequent shrinkage of hepatocytes in DL, could explain this finding even though no change in mean hepatocyte volume was observed in stereological evaluations after 1 week postoperative. Additionally, mean

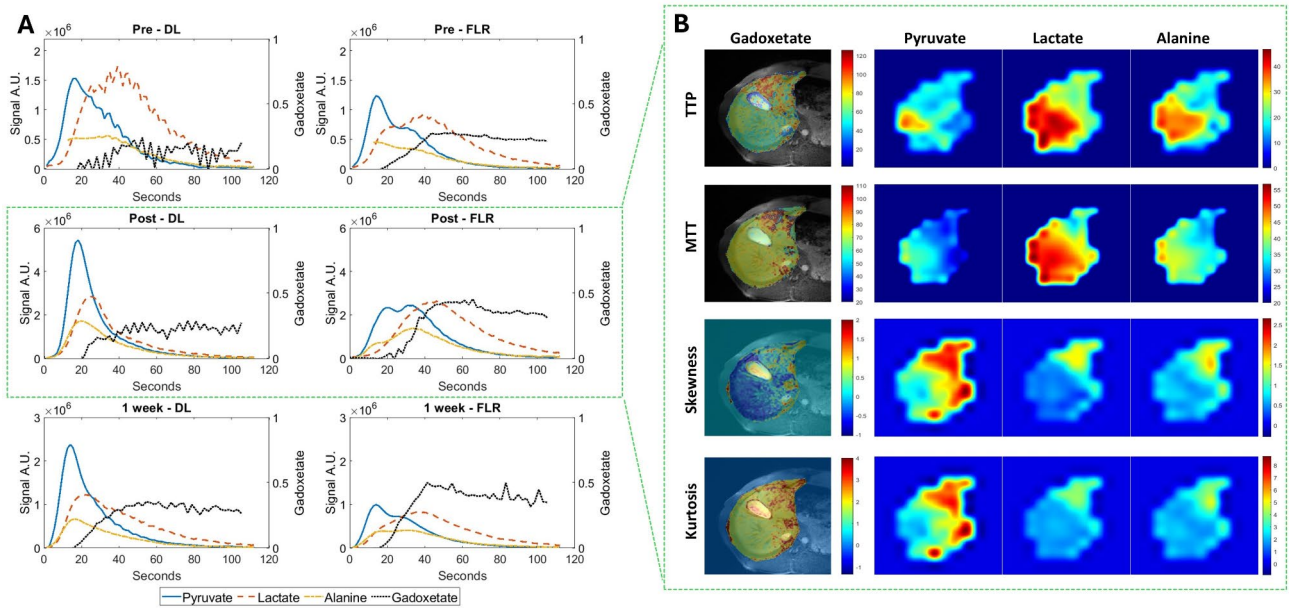

Fig. 4. Dynamic signal intensity curves and hemodynamic maps. (**A**) Region of interest time curves for DL (left column) and FLR (right column) showing metabolic dynamics pre, post and 1 week after surgery in one pig. Signal intensity shown in arbitrary units (A.U) not corrected for different flip angels. Signal intensity of Gadoxetate is shown on the right y-axis (A.U). Note that pyruvate influx and build-up of lactate are prolonged in the FLR post-surgery and after 1 week, representing the preserved inflow from vena portae in the FLR. (**B**) TTP, MTT, skewness and kurtosis maps for gadoxetate and [1-^{13}C]-Products in the liver post-surgery. Gadoxetate is overlayed on T1-weigthed images. Data are from the same animal as in Fig. 1.

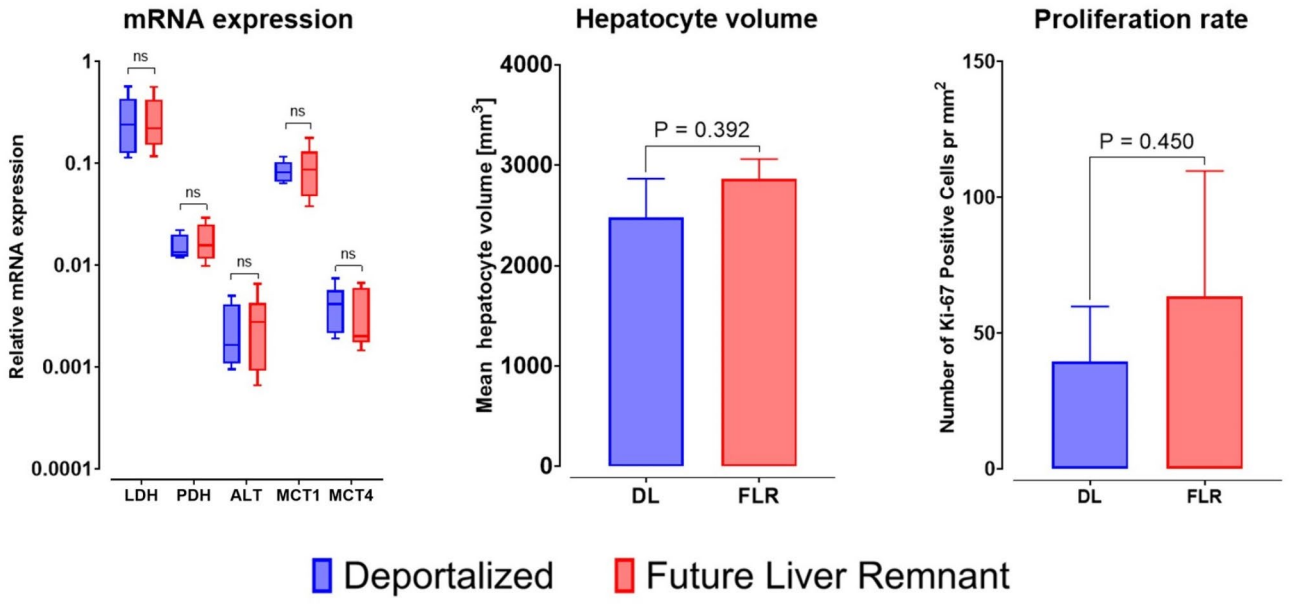

Fig. 5. Tissue analysis 1 week after PVL. Relative mRNA expression of membrane transporters and enzymes involved in pyruvate metabolism. Proliferation rate quantified by Ki-69 positive cells and estimated mean hepatocyte volume. Relative mRNA expression presented as boxplot. Tested with paired *t*-test.

hepatocyte volume only quantifies intracellular volume, while a change in extracellular volume would also affect mean ADC value.

Increased lactate production in the FLR is driven by cellular reprogramming

The increase in lactate production observed in our study shows a metabolic shift towards increased lactate production in the FLR, reflecting the enhanced glycolytic activity required to support the regenerative process. While quiescent or normal cells rely mainly on oxidative metabolism, proliferating cells have an increased need for biomass, and consequently, the cells' metabolism is reprogrammed, resulting in increased lactate production[7,31]. Interestingly this metabolic reprogramming was detectable by HP-MRI immediately after surgery.

In a mouse model of 70% partial hepatectomy, no change in pyruvate to lactate conversion was observed between controls and 70% partial hepatectomy on postoperative day 3. However, when blocking the cell division, a shift to increased ALT activity was observed[32]. The same study observed an increase in the NADH to NAD^+ ratio following liver regeneration. This change in redox state, which is a consequence of the metabolic reprogramming in proliferation cells, could be responsible for the increased lactate production found in our study, as NAD^+ and NADH are pivotal co-enzymes in pyruvate to lactate conversion. It has been suggested that increased lactate production in cancer cells is a compensatory mechanism for excessive NADH production in the mitochondria of proliferation cells[33,34]. Together, this strongly suggest that the increased lactate production observed in the FLR is likely a synergistic effect of an altered redox state, driven by changes in the NADH/NAD^+ ratio, combined with an increased intracellular lactate concentration in regenerating hepatocytes. The slightly higher increase in k_{PL} post-surgery compared to 1 week after could be explained by collateralization of portal vein supply, as shown in a previous pig model of PVL[35]. Previously, studies found that HP-MRI pyruvate to lactate conversion is rate limited by the MCT1 expression in both ex vivo and in vivo tumor cells[36,37] where our results indicate that this is not necessarily the case for normal hepatocytes in vivo, which may instead be explained by changes in pyruvate perfusion acting as the rate-limiting factor in the DL and FLR. The absence of an increase in alanine flux in our PVL model suggests that transamination is not significantly affected during liver regeneration. However, whether this holds true in more pronounced regeneration models, such as partial hepatectomy, or in human liver regeneration remains to be determined.

Liver regeneration was not confirmed in the PVL model through direct measures of proliferation, hepatocyte volume, and mRNA expression, all of which remained unaltered 1 week post-surgery. Deal et al.[38] reported increased Ki-67 index in the FLR in pig model of PVL when comparing baseline histology and seven days after surgery, however the same group were unable to replicate their findings in a later study[39]. This lack of significant changes in key indicators of liver regeneration suggests that the regenerative response in our study may have either peaked earlier or was not adequately stimulated. The former is consistent with proliferation after partial hepatectomy in rodents typically peaks after 24 h and returns to baseline levels after 72–120 h[5,40]. If the latter is the case, the observed metabolic lactate conversion should be attributed to changes in blood flow. However, the increase in ADC in the DL after 1 week argues against this, suggesting that the metabolic change to a glycolytic shift observed post-surgery is mainly driven by increased demand for building blocks in proliferation cells[7]. The metabolic increase in the FLR may be a consequence of the need to adapt its functionally to meet the higher demands required to maintain body homeostasis. The observed discrepancy between HP MRI and gene expression, proliferation rate, and cell volume indicates that metabolic shifts occur before structural and molecular changes become apparent. This underscores the potential of HP MRI as an early and non-invasive biomarker of liver regeneration, offering real-time metabolic insights without requiring biopsies.

Our immunohistochemical analysis did not allow for the visualization of immune cells, limiting our ability to assess inflammatory cell infiltration, that previously has shown to contribute to increased lactate production in the liver[41] and in the brain[42,43]. However, previous studies have shown no presence of inflammatory cells in the deprived portal liver lobe seven days after PVL. Additionally, biochemical analysis demonstrated that all liver-specific markers were not significantly elevated post-surgery and returned to baseline by postoperative day 7[39]. Given that pro-inflammatory cytokines primarily act to initiate regeneration and normalize within days[40], it is unlikely that activity from inflammatory cells played a major role in the metabolic changes observed at this time point. Moreover, as lactate production was comparable in both FLR and DL immediately post-surgery and at 1 week, it is unlikely that immune cell metabolism was a major contributor. Instead, the observed lactate production is more plausibly linked to the regenerative processes in hepatocytes.

Despite the inability to confirm liver regeneration with stereology, we observed a decrease in ADC in the FLR, which likely reflects a relatively larger increase in intracellular volume compared to extracellular volume. This finding indicates some level of cellular response that was most pronounced after 1 week.

The increased lactate production observed in the FLR following PVL may be influenced by lactate recycling through the portal vein. Under normal conditions, the liver receives blood through a dual-input system comprising the portal vein and hepatic artery, which facilitates efficient nutrient and metabolite processing, including lactate clearance. However, after PVL, the DL shifts to single blood supply, relying solely on the hepatic artery, while the FLR continues to receive dual blood supply. This altered hemodynamics could enhance the lactate signal in the FLR, partly due to lactate influx from the intestines, spleen, and pancreas via the portal vein. This shift may lead to a higher local concentration of lactate and contribute to the observed rise in k_{PL}. If this is the case, it could lead to an overestimation of k_{PL}. However, it is likely that the altered blood flow and the ongoing metabolic demands of regeneration synergize to elevate lactate production in the FLR. Previous studies have suggested that the lactate shuttle interferes with metabolic conversion of HP-MRI in the brain[44]. While the glucose-lactate shuttle between extrahepatic tissue and the liver is generally accepted[45,46], whether it affects the HP-MRI signal in the liver needs to be further elucidated. The extent to which altered blood flow contributes to the observed metabolic changes remains uncertain. Future studies could investigate this by

assessing how changes in liver perfusion, for example, through the acute effects of splanchnic vasoconstrictors such as vasopressin, influence pyruvate to lactate conversion.

This study presents several limitations that should be considered when interpreting the results. First, the small sample size limits the statistical power and generalizability of the findings. Additionally, a sham group could have strengthened the findings by assessing anesthesia and surgical effects, but since the primary aim was to compare metabolic changes between FLR and DL, these effects likely influenced both regions similarly. Second, the spectral resolution and potential partial volume effects inherent in hyperpolarized [1-^{13}C] pyruvate MRI could affect the accuracy of the metabolic measurements. Third, breathing motion during imaging can introduce artifacts, despite efforts to mitigate this through mechanical ventilation and breath-hold.

In conclusion, HP-MRI was able to detect intrahepatic metabolic changes within hours following PVL in a porcine model, while RLE in the hepatobiliary phase of gadoxetate disodium did not change. This underlines the potential of adding HP-MRI to the preoperative assessment of liver function before major partial hepatectomy, thereby enabling more tailored surgical planning and risk stratification, ultimately reducing the incidence of PHLF and associated morbidity and mortality. This advance not only enhances the safety of surgical interventions but also broadens the eligibility for liver resections among patients previously deemed high-risk. Future studies should prospectively assess metabolic liver function using HP-MRI in patients at risk of PHLF before surgery (Fig. 6C).

Declaration of AI and AI-assisted technologies in the writing process

During the preparation of this work the authors used ChatGPT4.0 support in order to proofread the manuscript. After using this tool/service, the authors reviewed and edited the content as needed and take full responsibility for the content of the publication.

Methods

Animal handling

All experimental protocols were approved by the Danish Animal Experiments Inspectorate (License 2018-15-0201-01530) and were conducted in accordance with the relevant national and institutional guidelines and regulations, including the ARRIVE guidelines. Six female pigs (Yorkshire, Danish domestic crossbreds), each weighing 40.5–43.9 kg, were included in this study. Pigs underwent HP-MRI and MRI scans pre-, post- (220–323 min), and 1 week (6–8 days) after surgery (Fig. 6A).

The pigs were fed a restricted diet (Svin Foder VAK, Danish Agro, Denmark) and tap water ad libitum. They were housed in 12/12 h of light/darkness at 20–22 °C and approximately 55% humidity. After an overnight fast, pigs were sedated with an intramuscular injection of zoletilemix (0.1 ml/kg), containing tiletamine (12.5 mg/ml), zolazepam (12.5 mg/ml), ketamine (12.5 mg/ml), xylazine (12.5 mg/ml), and butorphanol (2.5 mg/ml). Two catheters were inserted into ear veins for intravenous administration of medication and for injection of hyperpolarized [1-^{13}C] pyruvate and gadoxetate disodium. The pigs were intubated and mechanically ventilated, aiming at an end-tidal CO_2 of 5.5 kPa. Anesthesia was maintained with propofol (~ 8 mg/kg/h) and fentanyl (~ 12.5 µg/kg/h). The pigs were then transported to the MRI scanner. At the end of the experiment the pigs were euthanized with an intravenous overdose of pentobarbital.

Surgical procedure

A midline laparotomy was performed. The hepatoduodenal ligament was dissected, and the portal vein was identified. The pig liver consists of five lobes, left medial (LM), left lateral (LL), right medial (RM), right lateral (RL) and caudate lobe (CL), each lobe has an individual dual input from branches of the hepatic artery and the portal vein (Fig. 6B)[47]. Branches of the portal vein were identified, and the main left branch of the portal vein was ligated (Fig. 6A), resulting in deportalization of LL, LM and RM. The FLR, consisting of the RL and the CL, accounted for approximately 26% of the total liver volume[48]. After ligation, deportalization was confirmed visually by the presence of cyanosis in the affected lobes. For antibiotic prophylaxis, 1 g of ampicillin was administered i.v. For preoperatively pain relief, 0.6 mg of Buprenorphine was given i.v., and Metacam was administered i.m. daily for five days.

Magnetic resonance imaging

A 3T MRI scanner (Discovery MR750, GE Healthcare, Wisconsin, USA) was used for both ^{1}H and HP-MRI scans. A 16-channel flexible coil (GE Healthcare, Milwaukee, USA) and the integrated body coil were used for proton imaging. T1-weigthed dual-echo spoiled gradient echo imaging (Field of view (FOV) = 40 × 40 cm, matrix = 256 × 256, echo time (TE) = 2.2 ms/1.1 ms, repetition time (TR) = 1.7 ms, slice thickness 5.0 mm (interpolated from 10 mm), flipangle = 15 degree) was obtained with arrested respiration in the oblique plane consisting of 48 slices to ensure full liver coverage. These images were used for the slice selection for the subsequent ^{13}C imaging. Apparent diffusion coefficient (ADC) maps were fitted from diffusion weighted images (DWI) that was acquired respiratory gated with the following parameters (FOV = 40 × 40 cm, matrix = 128 × 96, TE = 55.8 ms, TR = 15,000 ms, flip angle = 90°, slice thickness 5.0 mm, b-values = 0, 50, 400, 800 with NEX = 1, 1, 2, 4, respectively). All ^{1}H images acquired in the axial plane were automatically moved into the space of ^{13}C images using the image registration tool in ITK-SNAP (version 4.2.0) to ensure accurate overlay before region of interest (ROI) analysis[49].

Dynamic contrast enhancement

For assessment of perfusion, dynamic contrast enhancement (DCE) was performed following an i.v. injection of gadoxetate disodium (0.025 mmol/kg at ~ 5 mL/s, followed by a 20 ml saline flush) with a 3D spoiled gradient echo (TR = 4.1 ms, TE = 1.7 ms, matrix = 160 × 160, FOV = 36 × 36 cm, flip angle = 12 degrees, dynamic

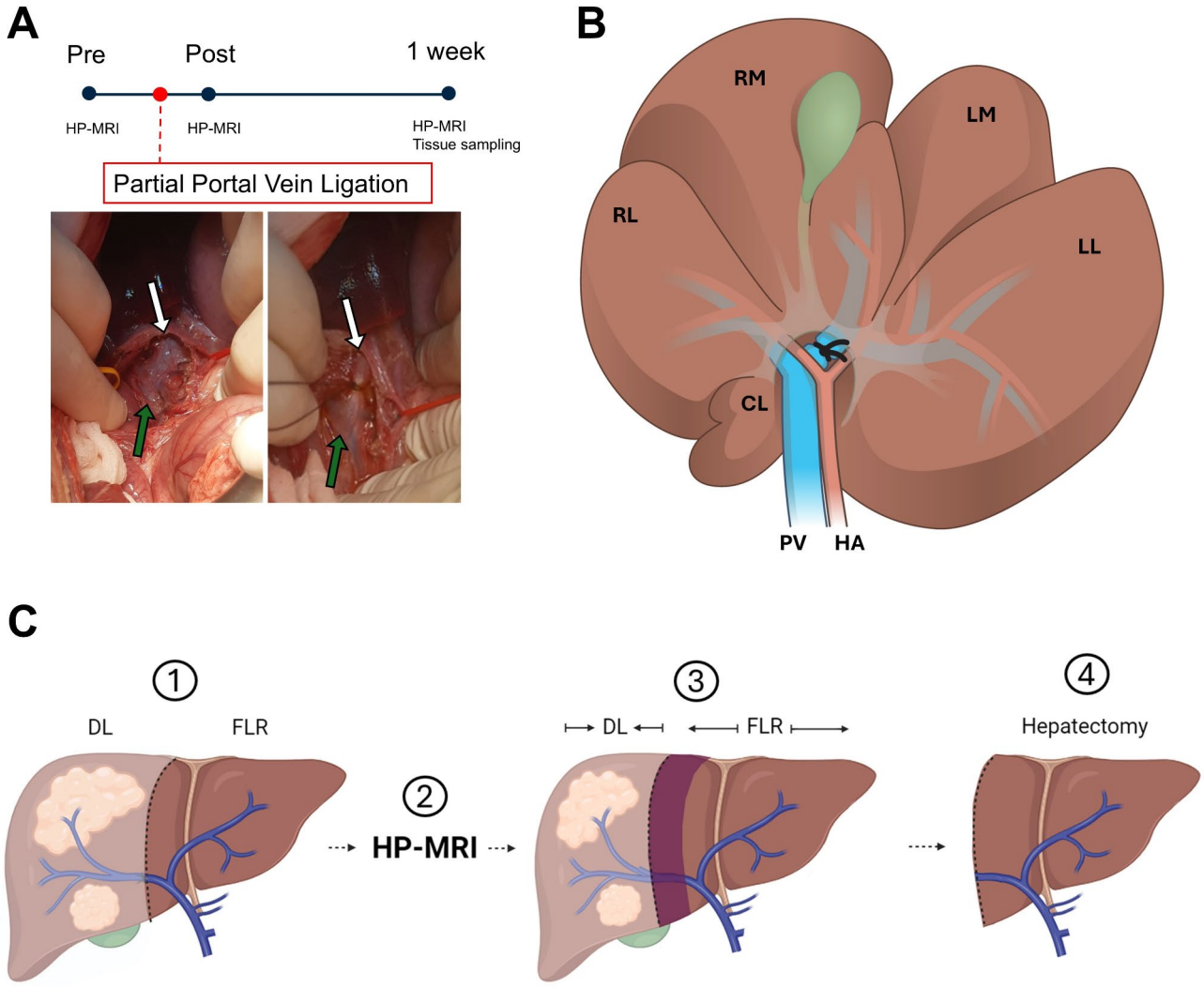

Fig. 6. Study overview and regional metabolic assessment of liver function with HP-MRI. (**A**) Study timeline. Before and after partial portal vein ligation. Green Arrow: portal vein. White arrow: common branch of portal vein supplying RM, LM and LL. (**B**) Caudoventral view of the pig liver with ligation of common branch of the portal vein. (**C**) Proposed clinical workflow of assessment of metabolic liver function in the FLR by HP-MRI. (1) Manipulation of hepatic blood flow to promote regeneration in the FLR. (2) Assessment of metabolic liver function by HP-MRI. (3) Volumetric measurement of FLR by CT or MRI, purple area shows hypertrophy. (4) Hepatectomy. To ensure optimal clinical workflow HP-MRI can be done in combination with step (1) or (3) RM, right medial; LM, left medial; LL, left lateral; RL, right lateral; CL, caudate lobe; PV, portal vein; HA, hepatic artery; FLR, future liver remnant; DL, deportalized liver; HP-MRI, hyperpolarized magnetic resonance imaging. The authors thank Ken Peter Kragsfeldt for the illustrative work in (**B**). (**C**) was created with biorender.com.

resolution = 2.2 s, dynamic scans = 51). Injection was initiated ~ 4.4 s after image acquisition starting with the first 30 s involving a breath hold, for a total scan time of 112 s. T1-weighted dual-echo spoiled gradient echo imaging (FOV = 40 × 40 cm, matrix = 256 × 256, TE = 2.2 ms/1.1 ms, TR = 1.7 ms, slice thickness 5.0 mm (interpolated from 10 mm), flipangle = 15 degree) were acquired prior to and 20 min after gadoxetate disodium injection to calculate relative liver enhancement (RLE)[28]. All dual echo spoiled gradient echo imaging were reconstructed in in-phase, out-phase, fat and water weighted images. Only water images were used for analysis.

Hyperpolarized MRI

For HP-MRI a clamshell transmit coil (RAPID Biomedical, Rimpar, Germany) was used together with custom-made receiver coils (8 channel or 16 channel flexible surface coils, JD coils, Hamburg, Germany). The receiver coil was wrapped around the abdomen to ensure full coil coverage of the liver. An automated Bloch-Siegert shift was used to adjust center frequency. Imaging of [1-^{13}C] pyruvate, [1-^{13}C] lactate, [1-^{13}C] alanine and [1-^{13}C] bicarbonate were obtained by a dynamic 2D spectral-spatial (SPSP) acquisition with a spiral readout, as described previously[50]. Imaging was obtained in an oblique plane to match the anatomical positioning of the liver and ensure optimal receiver coil coverage. Scan parameters were 20 mm slice thickness, TR = 350 ms, TE = 10

ms, FOV = 24 × 24 cm (n = 2); 40 × 40 cm (n = 16) and flip angles of 12 degrees for pyruvate and 70 degrees for its metabolites. Images were acquired in the following repetition scheme; pyruvate, lactate, bicarbonate, and alanine with 350 ms between each metabolite. Acquisition began after the end of pyruvate injection, starting with the first 30 s involving a breath hold, for a total scan time of 112 s.

Hyperpolarization of pyruvate

Dynamic nuclear polarization of [1-^{13}C]-Pyruvic acid (Sigma-Aldrich) was done in a commercial system for > 1 h (SpinAligner, Polarize, Frederiksberg, Denmark) or > 2 h (SPINlab, GE healthcare, Chicago Illinois, USA) to ensure high polarization levels (typically 30–40%). Subsequently, the sample was dissolved and neutralized to a final concentration of 180 mM [1-^{13}C]-Pyruvic acid in volume of approximately 18 mL (Spin Aligner) or 29 ml (SPINlab). Time from dissolution to end of injection was < 30 s, with an injection time ~ 5 s. Injection of pyruvate was followed by 20 ml saline flush. For quality assurance, a liquid polarization test was performed using a 60-MHz benchtop NMR spectrometer (Spinsolve 60 Ultra, Magritek, Wellington, New Zealand). Polarization levels ranged from 22 to 67% (mean = 42.9%, n = 14).

Data processing

HP-MRI data were gridded, Fourier transformed, denoised[51,52] and partial volume corrected in Matlab (R2023a, Mathworks Inc, Natick, MA). All datasets were visually inspected for spiral artifacts. These were observed in some of the alanine images and consequently these timepoints were manually omitted from further analysis. Monoexponentially fitting of pyruvate to lactate conversion (k_{PL}) and pyruvate to alanine conversion (k_{PA}) maps were calculated with an input less two-site exchange model using the Hyperpolarized MRI toolbox[53]. A signal to noise ratio (SNR) mask of 2.5 for lactate was used for selection of which voxels to fit. Initial fitting parameters were set to: k_{PL} = 0.02, k_{PA} = 0.01, and T_1 relaxations rates of pyruvate, lactate, and alanine were set to 30, 25, and 25 s, respectively[27]. In two injections, a very low alanine signal was detected, while pyruvate and lactate signal was acceptable and therefore included in analysis. Both injections were in the same pig.

Image analysis

Regions of interest (ROIs) were drawn on the T1-weigthed images in Matlab. ROIs for DL and FLR were drawn on two oblique slices each with a distance from other organs, the abdominal wall, and large vessels to avoid partial volume effects (Fig. 1A). HP-MRI images were linearly interpolated to match the in-plane resolution of T1-weigthed images before ROI analysis. Mean ROI values were calculated for parametric HP-MRI maps and for raw signal intensity maps to compare dynamic time curves in the DL and FLR. RLE was calculated as the relative increase in signal on T1-weigthed images 20 min after gadoxetate disodium injection vs. pre-contrast images.

Hemodynamic analysis

Due to the liver's dual blood supply, with approximately 75% coming from the portal vein and only 25% coming from the hepatic artery[54], we decided to assess hemodynamic changes after PVL. Therefore, time to peak (TTP) and mean transit time (MTT) from the signal intensity curves of pyruvate, lactate, alanine, and gadoxetate disodium were quantified using the Hyperpolarized MRI toolbox[53]. We included MTT of lactate and alanine, as it reflects first order kinetics of conversion from pyruvate[55–57]. Furthermore, skewness and kurtosis were used to analyze the distribution and characteristics of the signal intensity curves using the Statistics and Machine Learning Toolbox in MATLAB. Seven seconds of the initial signal intensity curves for gadoxetate were omitted for analysis to correct for the mismatch in acquisition timing between DCE and HP-MRI.

Tissue samples

Immediately after euthanization, two tissue samples were collected from both the DL and the FLR. One sample was cut into pieces of approximately 1 mm^3, snap frozen in liquid nitrogen, and stored at − 80 °C before mRNA analysis (see below). The other sample was fixed in 4% formaldehyde for 24–48 h, stored at 4 °C in phosphate buffered saline and subsequently cut into 2-mm thick parallel slices using a tissue slicer. Tissue slices were then placed with the same side up and embedded in paraffin. Three 3-µm thick sections were cut from each paraffin-embedded block, ensuring systematic, uniform and random sampling for immunostaining and further stereological analysis.

Stereology

Immunohistochemical staining of the serial sections was performed using an in-house protocol described in a previous study[58]. In brief, monoclonal anti Ki-67 specific antibody (clone 30-9, Ventana Medical Systems, Roche, Basel Switzerland) was used as a proliferation marker, and anti-beta-catenin antibody (clone β-Catenin-1; Agilent Technologies, Santa Clara, CA, US) was used as a hepatocyte cell surface marker. All sections were counterstained with haematoxylin.

A blinded investigator analyzed all sections using an Olympus BX50 microscope modified for stereology using a motorized stage (Märzhäuser Wetzlar MFD, Wetzlar, Germany) and digital camera (Olympus DP73, Olympus, Tokyo, Japan), connected to a computer running newCAST version 2020.08.4.9377 software (Visiopharm, Hørsholm, Denmark). Three thin serial sections were used to estimate the total number of Ki-67-positive hepatocyte nuclei profiles per unit area of liver tissue, and hepatocyte volumes were estimated on hepatocytes with a beta-catenin-stained brown cell membrane. Counting rules and stereological probes are described in detail in a previous study[58].

RNA extraction and quantitative PCR

Total RNA was isolated from the liver tissue samples using the NucleoSpin RNA II mini kit according to the manufacturer's instructions (AH Diagnostics, Aarhus, Denmark). RNA was quantified by spectrophotometry and stored at −80 °C. cDNA synthesis was performed with the RevertAid First-Strand cDNA Synthesis Kit (Life Technologies, Thermo Fisher Scientific, Cambridge, MA, USA). qPCR was performed using Maxima SYBR Green qPCR Master Mix according to the manufacturer's instructions (AH Diagnostics). Briefly, 100 ng of cDNA was used as template for PCR amplification. The reaction was run on an Aria Mx3000P qPCR System (Agilent Technologies, Santa Clara, CA, USA). Specificity of products was confirmed by melting curve analysis and by gel electrophoresis. The primer sequences used are given in Supplementary Materials and methods; Table S1. Enzymes involved in pyruvate conversion to lactate (LDH), alanine (ALT), and bicarbonate (PDH) were selected, along with monocarboxylate transporters (MCT1 and MCT4), responsible for the intracellular uptake and release of pyruvate.

Statistics

All statistics were performed in GraphPad Prism version 10.0.0 for Windows (GraphPad Software, Boston, Massachusetts USA). Normality and lognormality were assessed with QQ-plots. If the data did not follow a normal distribution, a log transformation was applied to normalize it, followed by analysis, before log transforming it back. For comparison, linear mixed effects models were used to test effect over time and between liver regions with animals as a random effect. P-values reported are for interaction effects for time and liver regions, if not stated otherwise. For tissue and stereology comparisons, paired *t*-tests were used. Data are presented as means with SEM, if not stated otherwise.

Data availability

Data and code are available from the corresponding author upon request.

Received: 6 January 2025; Accepted: 10 March 2025
Published online: 26 March 2025

References

1. Poon, R. T., Yeung, C. & Wong, J. Improving perioperative outcome expands the role of hepatectomy in management of benign and malignant hepatobiliary diseases analysis of 1222 consecutive patients from a prospective database. https://doi.org/10.1097/01.sla.0000141195.66155.0c (2004).
2. Jarnagin, W. R. et al. Improvement in perioperative outcome after hepatic resection analysis of 1,803 consecutive cases over the past decade. *Ann. Surg.* **236**, 397–407 (2002).
3. Van Den Broek, M. A. J. et al. Liver failure after partial hepatic resection: definition, pathophysiology, risk factors and treatment. *Liver Int.* **28**, 767–780 (2008).
4. Rahbari, N. N. et al. Posthepatectomy liver failure: a definition and grading by the international study group of liver surgery (ISGLS). *Surgery* **149**, 713–724 (2011).
5. Michalopoulos, G. K. Liver regeneration. *J. Cell. Physiol.* **213**, 286–300 (2007).
6. Taub, R. Liver regeneration: from myth to mechanism. *Nat. Rev. Mol. Cell. Biol.* **5**, 836–847 (2004).
7. Heiden, M. G. V., Cantley, L. C. & Thompson, C. B. Understanding the Warburg effect: the metabolic requirements of cell proliferation. *Science* **324**, 1029 (2009).
8. Clavien, P. A., Petrowsky, H., Deoliveira, M. L. & Graf, R. Strategies for safer liver surgery and partial liver transplantation. *N. Engl. J. Med.* **356**, 1545–1559 (2007).
9. Schnitzbauer, A. A. et al. Right portal vein ligation combined with in situ splitting induces rapid left lateral liver lobe hypertrophy enabling 2-staged extended right hepatic resection in small-for-size settings. *Ann. Surg.* **255**, 405–414 (2012).
10. Khan, A. S. et al. Assessment and optimization of liver volume before major hepatic resection: current guidelines and a narrative review. *Int. J. Surg.* **52**, 74–81 (2018).
11. Guglielmi, A., Ruzzenente, A., Conci, S., Valdegamberi, A. & Iacono, C. How much remnant is enough in liver resection? *Dig. Surg.* **29**, 6–17 (2012).
12. Schroeder, R. A. et al. Predictive indices of morbidity and mortality after liver resection. *Ann. Surg.* **243**, 373–379 (2006).
13. Schneider, P. D. Preoperative assessment of liver function. *Surg. Clin. North Am.* **84**, 355–373 (2004).
14. Stockmann, M. et al. The LiMAx test: a new liver function test for predicting postoperative outcome in liver surgery. *HPB* https://doi.org/10.1111/j.1477-2574.2009.00151.x (2010).
15. De Gasperi, A., Mazza, E. & Prosperi, M. Indocyanine green kinetics to assess liver function: ready for a clinical dynamic assessment in major liver surgery? *World J. Hepatol.* **8**, 355–367 (2016).
16. Schwarz, C. et al. The value of indocyanine green clearance assessment to predict postoperative liver dysfunction in patients undergoing liver resection. *Sci. Rep.* https://doi.org/10.1038/s41598-019-44815-x
17. de Graaf, W. et al. Assessment of future remnant liver function using hepatobiliary scintigraphy in patients undergoing major liver resection. *J. Gastrointest. Surg.* **14**, 369–378 (2010).
18. Araki, K. et al. Functional remnant liver volumetry using Gd-EOB-DTPA-enhanced magnetic resonance imaging (MRI) predicts post-hepatectomy liver failure in resection of more than one segment. *HPB (Oxford)* **22**, 318–327 (2020).
19. Kim, D. K. et al. Prediction of posthepatectomy liver failure: MRI with hepatocyte-specific contrast agent versus indocyanine green clearance test. *Am. J. Roentgenol.* **211**, 580–587 (2018).
20. Theilig, D. et al. Predicting liver failure after extended right hepatectomy following right portal vein embolization with Gadoxetic acid-enhanced MRI. *Eur. Radiol.* **29**, 5861–5872 (2019).
21. Ardenkjaer-Larsen, J. H. et al. Increase of signal-to-noise of more than 10,000 times in liquid state NMR. *Discov. Med.* **3**, 37–39 (2003).
22. Moon, C. M. et al. Metabolic alterations in a rat model of hepatic ischaemia reperfusion injury: in vivo hyperpolarized ^{13}C MRS and metabolic imaging. *Liver Int.* **38**, 1117–1127 (2018).
23. Hu, S. et al. Use of hyperpolarized [1-^{13}C]pyruvate and [2-^{13}C]pyruvate to probe the effects of the anticancer agent Dichloroacetate on mitochondrial metabolism in vivo in the normal rat. *Magn. Reson. Imaging* **30**, 1367–1372 (2012).
24. Lee, P. et al. In vivo hyperpolarized carbon-13 magnetic resonance spectroscopy reveals increased pyruvate carboxylase flux in an insulin-resistant mouse model. *Hepatology* **57**, 515–524 (2013).
25. Kjærgaard, U. et al. Hyperpolarized [1–^{13}C] pyruvate as a possible diagnostic tool in liver disease. *Physiol. Rep.* **6**, e13943 (2018).

26. Lee, P. M. et al. Specialized computational methods for denoising, B1 correction, and kinetic modeling in hyperpolarized ^{13}C MR EPSI studies of liver tumors. *Magn. Reson. Med.* https://doi.org/10.1002/MRM.28901 (2021).
27. Lee, P. M. et al. Whole-abdomen metabolic imaging of healthy volunteers using hyperpolarized [1-^{13}C]pyruvate MRI. *J. Magn. Reson. Imaging*. https://doi.org/10.1002/JMRI.28196 (2022).
28. Poetter-Lang, S. et al. Quantification of liver function using Gadoxetic acid-enhanced MRI. *Abdom. Radiol.* **45**, 3532–3544 (2020).
29. Choi, J. Y., Lee, J. M. & Sirlin, C. B. CT and MR imaging diagnosis and staging of hepatocellular carcinoma: part I. Development, growth, and spread: key pathologic and imaging aspects. *Radiology* **272**, 635–654 (2014).
30. Pedro Filipe, J., Curvo-Semedo, L., Casalta-Lopes, J., Cristina Marques, M. & Caseiro-Alves, F. Diffusion-weighted imaging of the liver: usefulness of ADC values in the differential diagnosis of focal lesions and effect of ROI methods on ADC measurements. *MAGMA*. https://doi.org/10.1007/s10334-012-0348-1
31. DeBerardinis, R. J., Lum, J. J., Hatzivassiliou, G. & Thompson, C. B. The biology of cancer: metabolic reprogramming fuels cell growth and proliferation. *Cell. Metab.* **7**, 11–20 (2008).
32. Caldez, M. J. et al. Metabolic remodeling during liver regeneration. *Dev. Cell* **47**, 425–438e5 (2018).
33. Wang, Y. et al. Saturation of the mitochondrial NADH shuttles drives aerobic Glycolysis in proliferating cells. *Mol. Cell* **82**, 3270 (2022).
34. Lu, J., Tan, M. & Cai, Q. The Warburg effect in tumor progression: mitochondrial oxidative metabolism as an anti-metastasis mechanism. *Cancer Lett.* **356**, 156 (2015).
35. Deal, R. et al. Rapid liver hypertrophy after portal vein occlusion correlates with the degree of collateralization between lobes—a study in pigs. *J. Gastroint. Surg.* **22**, 203–213 (2018).
36. Rao, Y. et al. Hyperpolarized [1-^{13}C]pyruvate-to-[1-^{13}C]lactate conversion is rate-limited by monocarboxylate transporter-1 in the plasma membrane. *Proc. Natl. Acad. Sci. USA* **117**, 22378–22389 (2020).
37. Harris, T., Eliyahu, G., Frydman, L. & Degani, H. Kinetics of hyperpolarized 13C1-pyruvate transport and metabolism in living human breast cancer cells. *Proc. Natl. Acad. Sci. USA* **106**, 18131 (2009).
38. Deal, R. et al. Rapid liver hypertrophy after portal vein occlusion correlates with the degree of collateralization between lobes—a study in pigs. *J. Gastrointest. Surg.* **22**, 203–213 (2018).
39. Schadde, E. et al. Simultaneous hepatic and portal vein ligation induces rapid liver hypertrophy: A study in pigs. *Surgery* **165**, 525–533 (2019).
40. Andersen, K. J. et al. The natural history of liver regeneration in rats: description of an animal model for liver regeneration studies. *Int. J. Surg.* **11**, 903–908 (2013).
41. Josan, S. et al. Assessing inflammatory liver injury in an acute CCl_4 model using dynamic 3D metabolic imaging of hyperpolarized [1-^{13}C]pyruvate. *NMR Biomed.* **28**, 1671–1677 (2015).
42. Josan, S. et al. Assessing inflammatory liver injury in an acute CCl 4 model using dynamic 3D metabolic imaging of hyperpolarized [1-^{13}C]pyruvate. *NMR Biomed.* https://doi.org/10.1002/nbm.3431 (2015).
43. Le Page, L. M., Guglielmetti, C., Najac, C. F., Tiret, B. & Chaumeil, M. M. Hyperpolarized 13 C magnetic resonance spectroscopy detects toxin-induced neuroinflammation in mice. *NMR Biomed.* **32**, e4164 (2019).
44. Bøgh, N. et al. Lactate saturation limits bicarbonate detection in hyperpolarized 13 C-pyruvate MRI of the brain. *Magn. Reson. Med.* **88**, 1170–1179 (2022).
45. Li, X. et al. Lactate metabolism in human health and disease. *Signal. Transduct. Target. Ther.* **7**, 1–22 (2022).
46. Brooks, G. A. The science and translation of lactate shuttle theory. *Cell. Metab.* **27**, 757–785 (2018).
47. Ntonas, A., Katsourakis, A., Galanis, N., Filo, E. & Noussios, G. Comparative anatomical study between the human and swine liver and its importance in xenotransplantation. *Cureus* **12** (2020).
48. Court, F. G. et al. Subtotal hepatectomy: a Porcine model for the study of liver regeneration. *J. Surg. Res.* https://doi.org/10.1016/j.jss.2003.08.007 (2004).
49. Yushkevich, P. A. et al. User-guided 3D active contour segmentation of anatomical structures: significantly improved efficiency and reliability. *NeuroImage* https://doi.org/10.1016/j.neuroimage.2006.01.015 (2006).
50. Schulte, R. F. et al. Saturation-recovery metabolic-exchange rate imaging with hyperpolarized [1-13 C] pyruvate using spectral-spatial excitation. *Magn. Reson. Med.* **69**, 1209–1216 (2013).
51. Olesen, J. L., Ianus, A., Østergaard, L., Shemesh, N. & Jespersen, S. N. Tensor denoising of multidimensional MRI data. *Magn. Reson. Med.* https://doi.org/10.1002/MRM.29478 (2022).
52. Christensen, N. V. et al. A user independent denoising method for x-nuclei MRI and MRS. *Magn. Reson. Med.* **90**, 2539–2556 (2023).
53. Larson, P. E. Z. et al. Investigation of analysis methods for hyperpolarized 13 C-pyruvate metabolic MRI in prostate cancer patients. *NMR Biomed.* https://doi.org/10.1002/nbm.3997 (2018).
54. Eipel, C., Abshagen, K. & Vollmar, B. Regulation of hepatic blood flow: the hepatic arterial buffer response revisited. *World J. Gastroenterol. WJG*. **16**, 6046 (2010).
55. Daniels, C. J. et al. A comparison of quantitative methods for clinical imaging with hyperpolarized 13 C-pyruvate. *NMR Biomed.* **29**, 387–399 (2016).
56. Grist, J. et al. Developing a metabolic clearance rate framework as a translational analysis approach for hyperpolarized 13 C magnetic resonance imaging. *Sci. Rep.* **13**, 1613 (123AD).
57. Mikkelsen, E. F. R. et al. Hyperpolarized [1-13 C]-acetate renal metabolic clearance rate mapping. *Sci. Rep.* **7**, 1–9 (2017).
58. Lund, A. et al. Biochemical and morphological responses to post-hepatectomy liver failure in rats. *Sci. Rep.* **13**, 13544 (123AD).

Acknowledgements

Duy Anh Dang, Tau Vendelboe and Mette Dalgaard are acknowledged for their laboratory expertise and assistance. Thanks to the animal caretakers at Påskehøjgaard for taking care of the pigs during the study. The authors thank Ken Peter Kragsfeldt for the illustrative work in Fig. 6B. Figure 6C was created with biorender.com.

Author contributions

Study design: UK, NB, ESH, KS, AKOA, FVM, and CL. Experiments: UK, AL, MR, MHK, MA, NB, LBB, AKOA, ESH, FVM. Data analysis: UK, AL, MR, LBB, ESH, and CL. Data interpretation: UK, AL, KS, MAO, DBV, LBB, ESH, FVM, and CL. Statistical analysis, and manuscript writing: UK, and CL. Critical revision of the manuscript: All authors.

Funding

This work was supported by the Danish Cancer Society (R279-A16251) and Aarhus University.

Declarations

Competing interests
The authors declare no competing interests.

Additional information
Supplementary Information The online version contains supplementary material available at https://doi.org/10.1038/s41598-025-93725-8.

Correspondence and requests for materials should be addressed to U.K.

Reprints and permissions information is available at www.nature.com/reprints.

Publisher's note Springer Nature remains neutral with regard to jurisdictional claims in published maps and institutional affiliations.